Empirical Photochemical Modeling of Saturn's Ionization Balance Including Grain Charging

E. Vigren [ORCID], J. Dreyer [ORCID], A. I. Eriksson [ORCID], F. L. Johansson [ORCID], M. Morooka [ORCID], and J.-E. Wahlund [ORCID]
Swedish Institute of Space Physics, Uppsala, Sweden; erik.vigren@irfu.se

Abstract

We present a semianalytical photochemical model of Saturn's near-equatorial ionosphere and adapt it to two regions ($\sim$2200 and $\sim$1700 km above the 1 bar level) probed during the inbound portion of Cassini's orbit 292 (2017 September 9). The model uses as input the measured concentrations of molecular hydrogen, hydrogen ion species, and free electrons, as well as the measured electron temperature. The output includes upper limits, or constraints, on the mixing ratios of two families of molecules, on ion concentrations, and on the attachment rates of electrons and ions onto dust grains. The model suggests mixing ratios of the two molecular families that, particularly near $\sim$1700 km, differ notably from what independent measurements by the Ion Neutral Mass Spectrometer suggest. Possibly connected to this, the model suggests an electron-depleted plasma with a level of electron depletion of around 50%. This is in qualitative agreement with interpretations of Radio Plasma Wave Science/Langmuir Probe measurements, but an additional conundrum arises in the fact that a coherent photochemical equilibrium scenario then relies on a dust component with typical grain radii smaller than 3 Å.

Unified Astronomy Thesaurus concepts: Saturn (1426); Planetary ionospheres (2185)

1. Introduction

Saturn's upper atmosphere was probed in situ during the proximal orbits of the Cassini mission in 2017. During all proximal orbits, the Radio Plasma Wave Science/Langmuir Probe (RPWS/LP) was operating, offering different means to extract the electron number density (e.g., Wahlund et al. 2018; Morooka et al. 2019; Persoon et al. 2019). Likewise, during all passages, the Ion Neutral Mass Spectrometer (INMS) operated such that the number density of neutral species, most importantly H_2, could be determined (e.g., Waite et al. 2018; Miller et al. 2020). Cassini's orbits 288 (perigee on 2017 August 14) and 292 (perigee on 2017 September 9) were special among orbits reaching below 2000 km above the 1 bar level, in the sense that they included measurements of light ($<$8 amu) ion species by the INMS (e.g., Waite et al. 2018). These orbits reached $\sim$1700 km above the 1 bar level at their closest approaches, which occurred just south of the equator.

A couple of studies have focused on orbits 288 and/or 292 and combined RPWS/LP and INMS ion and neutral data to test our understanding of Saturn's photochemistry or fill in gaps where existing measurements do not provide direct or definite answers. For instance, the ion measurements of INMS (Waite et al. 2018) are restricted to species with mass-to-charge ratios $<$8 Da, which essentially covers only H^+, H_2^+, H_3^+, and He^+ (and isotopic variants). For altitudes near 1700 km, the measured total number densities of these species are markedly lower than the electron and total ion number densities inferred from RPWS/LP measurements (Morooka et al. 2019), which leads to the obvious question of what species actually dominates the ion composition in this region. Dreyer et al. (2021) combined RPWS/LP ion (number density) and electron (number density and temperature) data with INMS H_2 and H_2^+

(number density) data to estimate an upper limit of the effective recombination coefficient at a reference electron temperature of 300 K. Comparing their derived upper limits with recombination rate constants measured in laboratories, they argued for a dominance of ion species characterized by comparatively low rate constants and raised HCO^+ as a prime suspect. This is at odds with predictions of H_3O^+ dominance from earlier model works (e.g., Moore et al. 2018). Considering the low proton affinity of CO in comparison to species like H_2O and NH_3 and the associated efficiency of proton transfer reactions like $HCO^+ + H_2O \rightarrow H_3O^+ + CO$ and $HCO^+ + NH_3 \rightarrow NH_4^+ + CO$, it is actually hard to imagine HCO^+ dominance in said region of the ionosphere unless the mixing ratio of CO markedly exceeds (an order of magnitude or so) those of H_2O, NH_3, and other species characterized by higher proton affinities than CO. On the one hand, the INMS analysis by Miller et al. (2020) of mixing ratios of different species in Saturn's upper atmosphere gives no obvious support for the idea of CO being more abundant than species like H_2O. On the other hand, Cravens et al. (2019) presented independent results, suggesting that the mixing ratio of CO (or CO-like molecules) exceeds that of, e.g., H_2O in Saturn's near-equatorial ionosphere. We return to the details of their study below and note merely, for the time being, that the work supports, at least indirectly, the idea of an ionosphere at least regionally dominated by HCO^+, as proposed by Dreyer et al. (2021).

However, the HCO^+ dominance proposed by Dreyer et al. (2021) is not carved in stone. To estimate the upper limit of the effective recombination coefficient, the total ion number density, as measured by the LP, enters the denominator in the formalism of Dreyer et al. (2021). This implies that an overestimated value of the ion number density would bring about too low of an estimate of the effective recombination coefficient. Around an altitude of $\sim$1700 km above the 1 bar level, the reported total ion number density for all flybys reaching such depths is markedly higher than the number density of free electrons (see Figure 6 of Morooka et al. 2019),

a feature suggesting significant electron depletion due to grain charging. While grains falling into Saturn's upper atmosphere have been suggested from model calculations to originate mainly from the B and C rings (Hsu et al. 2018), the flow into the near-equatorial upper atmosphere also has important contributions from the D ring (Mitchell et al. 2018). As noted by Dreyer et al. (2021), earlier Saturn ionospheric models did not work with the assumption that dust was ubiquitous enough to have any notable influence on the ionization balance. Even in some recent works (e.g., Moore et al. 2018; Cravens et al. 2019), authors have utilized the assumption that the total number density of gas-phase positive ions equals the number density of free electrons. Dreyer et al. (2021) merely noted that if, in their analysis, they had forced the ion number density to be equal to the measured number density of free electrons, the resulting effective recombination coefficient would be more compatible with an H_3O^+-dominated ionosphere.

One may speculate that secondary electron emission (from "ram neutrals" smashing into the LP at $>30\,km\,s^{-1}$) could contribute to the current on the ion side of the LP voltage sweeps and—when not accounted for—give the impression of higher ion number densities than actually present. For instance, a very strong secondary electron emission was reported for Giotto (and Vega I and Vega II) when flying through the water-dominated coma of comet 1P/Halley at $\sim 70\,km\,s^{-1}$ (Grard et al. 1987). Studies with the aim to estimate the actual contribution of secondary electron emission to the current on the ion side of the LP bias voltage sweeps performed in Saturn's ionosphere are therefore ongoing in parallel. In the present work, the total ion number density is, as explained below, merely an output parameter of a model.

To briefly return to and explain the work of Cravens et al. (2019), they drew awareness to the fact that in the deep ionosphere, the measured number density of H^+ locally exceeds that of H_3^+, despite the latter ion being produced at a rate ~ 10 times higher. This is not possible to explain solely (or predominantly) by the fact that H_3^+ reacts faster than H^+ with free electrons. Rather, Cravens et al. (2019) empirically calculated the mixing ratios of two types of molecules, labeled R and M, and showed that the H^+ and H_3^+ number densities in the deep ionosphere are compatible with a neutral background environment wherein locally, the mixing ratio of R-type molecules greatly exceeds that of M-type molecules. Now R- and M-type molecules are defined, respectively, as molecules "reacting with H_3^+ but not H^+" and "reacting with both H_3^+ and H^+." A survey of reaction databases like the UMIST database for astrochemistry (McElroy et al. 2013; see udfa.ajmarkwick.net) and the Kinetic Database for Astrochemistry (Wakelam et al. 2015; see kida.astrophy.u-bordeaux.fr) results in only a few plausible candidates for R-type molecules: essentially, CO and N_2. On the contrary, M-type molecules are numerous, and candidates include cosmically abundant molecules like H_2O, CH_4, NH_3, and CO_2. From Figure 4 in Cravens et al. (2019), it is seen that near the equatorial crossing of orbit 288, the empirically derived mixing ratio of R-type molecules exceeds 10^{-3}, while that of M-type molecules is only a few times 10^{-5}. This can again be contrasted with the results reported in Miller et al. (2020), who reported an average mixing ratio of a few times 10^{-4} for H_2O and overall higher average mixing ratios of M-type than of R-type molecules if translated into the nomenclature of Cravens et al. (2019).

It should be stressed that the method of Cravens et al. (2019) results in mixing ratios of R- and M-type molecules that vary along Cassini's trajectory. It is particularly at near-equatorial latitudes along the Cassini trajectory where the mixing ratios of R-type molecules grow significantly in comparison to M-type molecules. An interesting speculation by the authors is that the R-type molecules might be generated by ablation of grains entering the atmosphere. This is also touched upon by Yelle et al. (2018), who further noted that molecules liberated from micrometeorite bombardment are prone to recondense more or less effectively on particles of ring origin. They argued that cosmically abundant molecules with high vapor pressures, such as CO, can be expected to flow into Saturn's equatorial atmosphere.

In the present work, we make similar calculations as Cravens et al. (2019) but extend their photochemical reaction network in ways that allow predictions of additional parameters (most importantly, the total ion number density and the number density of specific ion types) while retaining the possibility of solving the system semianalytically. In contrast to Cravens et al. (2019), we do not enforce quasi-neutrality in the classical sense of $n_e = n_i$. Instead, we couple our ion chemistry model to the grain-charging formalism of Draine & Sutin (1987), which allows us to calculate the typical grain size needed for realizing a coherent photochemical equilibrium scenario that respects overall quasi-neutrality.

The outline of our paper is as follows. In Section 2, we present our model. In Section 3, we apply the model to two locations encountered during the inbound part of Cassini's orbit 292 and present both input and output parameters of the model. We proceed by discussing the findings with an emphasis on persisting conundrums. A summary with concluding remarks is given in Section 4.

2. Model Description

2.1. Brief Description

The inputs into the model are the electron number density n_e, the electron temperature T_e, and the concentrations of H_2, H^+, H_2^+, and H_3^+. The ion temperature is set equal to T_e by default but can be shifted. The model first calculates an upper limit for the concentration of M-type molecules (molecules like H_2O, NH_3, and CH_4 being reactive with both H^+ and H_3^+). The value of [M] is then stepped from close to zero to the upper limit, and for each fixed value of [M], the model calculates a range of parameters. These include, e.g., the concentration of R-type molecules (molecules like CO and N_2 being reactive with H_3^+ but not H^+) and the concentrations of ion species MH^+ and RH^+ (protonated versions of the M- and R-type molecules, e.g., H_3O^+ and HCO^+, respectively). Another output is the electron loss rate due to dust attachment. The model thus allows for solutions with the total gas-phase ion number density n_i exceeding n_e. As a final step in the model, the grain-charging theory of Draine & Sutin (1987) is incorporated to calculate the typical grain size needed to allow for a self-consistent solution of the ionization balance within the framework of photochemical equilibrium. Because a model run renders output parameters over ranges (rather than unique fixed values), we refrain from presenting along Cassini trajectory altitude profiles but rather focus on two separate regions encountered during the inbound part of Cassini's orbit 292 (see Sections 3.1 and 3.2).

2.2. Ion-electron Pair Production

Ion-electron pair production is conceived as driven by photoionization and electron-impact ionization of H_2 (e.g., $H_2 + h\nu \rightarrow H_2^+ + e^-$ or $H^+ + H + e^-$). The production rate of the $H_2^+ + e^-$ pair is assumed equal to the H_2^+ loss rate through its reaction with H_2 producing H_3^+ (written out, the reaction reads $H_2^+ + H_2 \rightarrow H_3^+ + H$). This loss rate is given by $k_{pt}[H_2^+][H_2]$, where $k_{pt} = 2.0 \times 10^{-9}$ cm^3 s^{-1} is the rate constant for the reaction. The above expression also represents the production rate of H_3^+, which we denote by p_3. The production rate of the $H^+ + e^-$ pair, p_1, is taken as a fraction γ of p_3. We adapt $\gamma = 0.20$ as a default value. This is set rather crudely and subject to further discussion below. In summary, the production rates of protons, H_3^+, and free electrons are calculated as
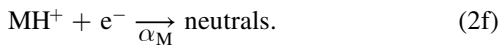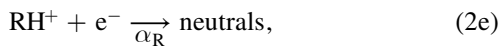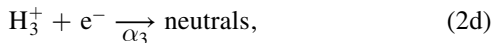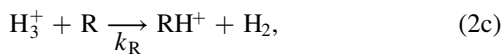
$$p_1 = \gamma k_{pt}[H_2^+][H_2], \tag{1a}$$
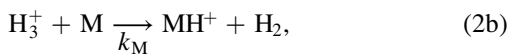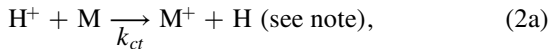
$$p_3 = k_{pt}[H_2^+][H_2], \tag{1b}$$

$$p_e = p_1 + p_3 = (1 + \gamma)k_{pt}[H_2^+][H_2], \tag{1c}$$

with $k_{pt} = 2.0 \times 10^{-9}$ cm^3 s^{-1} and $\gamma = 0.20$. Similar expressions are utilized by Cravens et al. (2019), although with $\gamma = 0.10$. Our selection of γ is based on Huebner & Mukherjee (2015) and the associated online tool phidrates.space.swri.edu suggesting γ in the range 0.17–0.25 (unattenuated solar extreme-UV branching fractions, depending on solar activity). We note that the γ values that may be read graphically from figures in the detailed works of Galand et al. (2009) and Kim et al. (2014) do not appear to exceed 0.10. We discuss the sensitivity of the model results to the selection of γ in Section 3.3.1.

2.3. Ion-neutral and Ion-electron Reactions

The following ion-neutral and recombination reactions are taken into consideration:

$$H^+ + M \xrightarrow{k_{ct}} M^+ + H \text{ (see note)}, \tag{2a}$$

$$H_3^+ + M \xrightarrow{k_M} MH^+ + H_2, \tag{2b}$$

$$H_3^+ + R \xrightarrow{k_R} RH^+ + H_2, \tag{2c}$$

$$H_3^+ + e^- \xrightarrow{\alpha_3} \text{neutrals}, \tag{2d}$$

$$RH^+ + e^- \xrightarrow{\alpha_R} \text{neutrals}, \tag{2e}$$

$$MH^+ + e^- \xrightarrow{\alpha_M} \text{neutrals}. \tag{2f}$$

Importantly, we assume that the M^+ produced in Equation (2a) is rapidly (on the order of a second) converted to MH^+ through a reaction with H_2. Guided by Cravens et al. (2019), we adapt $k_{ct} = 5.0 \times 10^{-9}$ and $k_M = 3.5 \times 10^{-9}$ cm^3 s^{-1}. Lead by rate constants listed on the UMIST database for astrochemistry (McElroy et al. 2013; see also udfa.ajmarkwick.net) for reactions of H_3^+ with CO or N_2, we utilize $k_R = 2.0 \times 10^{-9}$ cm^3 s^{-1}. Similar to Cravens et al. (2019), we do not consider a flow from RH^+ ions to MH^+ ions, or vice versa. The reason for this is that there are options for flow in both directions, and the flow direction will, as expanded upon in Section 4, depend critically on what actual species makes up the bulk of the M-type population. For instance,

CH_5^+ (MH^+ ion) can transfer a proton to CO (R neutral), while HCO^+ (RH^+ ion) can proton transfer to H_2O (M neutral). Rate constants for the recombination reactions are set to $\alpha_3 = 1 \times 10^{-7} \times (T_e/300 \text{ K})^{-0.70}$, $\alpha_M = 8 \times 10^{-7} \times (T_e/300 \text{ K})^{-0.70}$, and $\alpha_R = 2 \times 10^{-7} \times (T_e/300 \text{ K})^{-0.70}$ cm^3 s^{-1}, where T_e is the electron temperature. These values are set under the guidance of the laboratory results for the dissociative recombination of H_3^+, H_3O^+, NH_4^+, CH_5^+, HCO^+, and N_2H^+ (see, e.g., Table 1 in Dreyer et al. 2021) and, to some extent, by the modeling results of Moore et al. (2018).

2.4. Grain Attachment and Mass-corrected Ion Number Density

Our model does not enforce quasi-neutrality in the classical sense of $n_e = n_i$, where n_i denotes the total positive ion number density. Instead, ions, as well as electrons, are allowed to attach to dust particles. We assume the dust component to be in current balance, collecting electrons and ions at equal rates, and, as at $\sim$10 au, we ignore the photoelectric effect. Letting s_e and s_1 denote the inverse lifetimes of free electrons and protons against dust attachment, we enforce

$$s_e n_e = s_1\left([H^+] + \frac{[H_2^+]}{\sqrt{2}} \right.$$
$$\left. + \frac{[H_3^+]}{\sqrt{3}} + \frac{[MH^+]}{\sqrt{19}} + \frac{[RH^+]}{\sqrt{29}}\right) = s_1\theta_C. \tag{3}$$

The attachment rate of ions to a dust grain is inversely proportional to the square root of the ion mass. For instance, we could have let $s_3[H_3^+]$ denote the rate at which H_3^+ attaches to dust grains, but from the grain-charging formalism of Draine & Sutin (1987), it is clear that s_3 can be expressed as $s_3 = s_1/\sqrt{3}$. By Equation (3), we have also introduced θ_C, a mass-corrected ion number density useful (as shall be seen later) when modeling the grain charging in detail. Note that we assume the MH^+ and RH^+ ions to have characteristic masses of 19 and 29 amu, respectively. The mass selected for RH^+ ions should be fine, as thus far, we have only identified CO and N_2 as probable R-type molecules. Using 19 amu as characteristic mass for the MH^+ ions assumes this population to be dominated by H_3O^+, but we note that the masses of other candidate molecules, like CH_5^+ and NH_4^+ (17 and 18 amu, respectively), are not far off. We discuss in Section 3.3.1 the effect on the model results if we instead adapt a mass of several hundred amu for the MH^+ ions, which would be consistent with them being dominated by complex organic ions.

2.5. Procedure of Calculations

Balancing production and loss of H^+ gives rise to the equation

$$p_1 = k_{ct}[H^+][M] + s_1[H^+], \tag{4}$$

where p_1 is given by Equation (1a), [M] denotes the concentration of M-type molecules, and s_1 is the inverse lifetime for a proton against dust attachment. Already from Equations (1a) and (4), we can calculate an upper limit for the

mixing ratio of f_M simply by setting $s_1 = 0$. This gives

$$f_{M,\text{upper limit}} = \gamma \frac{k_{pt}[\text{H}_2^+]}{k_{ct}[\text{H}^+]}. \tag{5}$$

We proceed by stepping f_M from a value close to zero up to $f_{M,\text{upper limit}}$. For each fixed value of f_M (corresponding to a fixed value of [M]), we can calculate the associated values of all other output parameters in a step-by-step manner (and so generate the kind of figures that are shown in Section 3). First, with fixed [M], it is obvious that s_1 can be extracted from Equation (4). Balancing the production (see Equation (1b)) and loss of H_3^+ then leaves [R] to be determined from otherwise fixed/given quantities:

$$p_3 = [\text{H}_3^+]\left(k_M[\text{M}] + k_R[\text{R}] + \alpha_3 n_e + \frac{s_1}{\sqrt{3}}\right). \tag{6}$$

The term $s_1/\sqrt{3}$ appears in the parentheses for reasons emphasized in Section 2.4, and p_3 is given by Equation (1b). We continue analogously determining the connected concentrations of RH^+ and MH^+ via

$$k_R[\text{H}_3^+][\text{R}] = [\text{RH}^+]\left(\alpha_R n_e + \frac{s_1}{\sqrt{29}}\right) \tag{7}$$

and

$$[\text{M}](k_{ct}[\text{H}^+] + k_M[\text{H}_3^+])$$
$$= [\text{MH}^+]\left(\alpha_M n_e + \frac{s_1}{\sqrt{19}}\right). \tag{8}$$

The associated total ion number density is then calculated as

$$n_i = [\text{H}^+] + [\text{H}_2^+] + [\text{H}_3^+]$$
$$+ [\text{MH}^+] + [\text{RH}^+], \tag{9}$$

while the mass-corrected ion number density θ_C is calculated according to Equation (3). Equation (3) also gives the associated electron loss rate due to dust attachment, i.e., $s_e n_e$; this is a key quantity for connecting our ion chemistry scheme to the grain-charging formalism of Draine & Sutin (1987). Before describing that step, let us just note that another quantity of interest (for comparison with observations) is the harmonic mean ion mass, which can be calculated as

$$m_{i,\text{harm}} = \frac{n_i}{\frac{[\text{H}^+]}{1} + \frac{[\text{H}_2^+]}{2} + \frac{[\text{H}_3^+]}{3} + \frac{[\text{MH}^+]}{19} + \frac{[\text{RH}^+]}{29}} m_p, \tag{10}$$

where m_p is the proton mass.

We consider spherical dust grains of a single size that can be at most singly positively charged, while we set no strict limit on the maximum negative charge. We let E_+, E_0, E_{-1}, etc. denote the inverse lifetimes against electron attachment of dust grains in charge states $+1$, 0, -1, etc. Likewise, we let P_0, P_{-1}, P_{-2}, etc. denote the inverse lifetimes against ion attachment of dust grains (we enforce $P_+ = 0$). Letting n_+, n_0, n_{-1}, etc. denote the number density of grains in charge state $+1$, 0, -1, etc., we are facing an equation system

$$P_0 n_0 = E_+ n_+, \tag{11a}$$

$$P_{-1} n_{-1} = -E_+ n_+ + (E_0 + P_0) n_0, \tag{11b}$$

$$P_{-2} n_{-2} = -E_0 n_0 + (E_{-1} + P_{-1}) n_{-1}, \tag{11c}$$

etc., assuming each grain charge state to be in equilibrium.

It can be worked out (see, e.g., Mallik 2001) that for integers $k \geqslant 1$,

$$n_{-k} = n_+ \frac{E_+ E_0 E_{-1} \ldots E_{-(k-1)}}{P_0 P_{-1} \ldots P_{-k}}, \tag{12}$$

while $n_0 = n_+ E_+/P_0$. While the inverse lifetimes are given from the formalism of Draine & Sutin (1987) as described below, the value of n_+ needs to be adjusted so that the solution respects overall quasi-neutrality. This is taken care of via

$$n_+ = \frac{n_i - n_e}{-1 + \sum_{j=1}^m jf_j}, \tag{13}$$

where the sum goes over negative charge states (e.g., $j = 3$ is associated with grains in charge state -3), n_i is from Equation (9), and f_j (dimensionless) is given by

$$f_j \equiv \frac{E_+ E_0 E_{-1} \ldots E_{-(j-1)}}{P_0 P_{-1} \ldots P_{-j}}. \tag{14}$$

We have included an upper limit of $j = m$ for the sum in the denominator, mainly to emphasize that for practical consideration, it may in some cases not be necessary to consider particularly high values of j (for instance, for subnanometer grains, f_j becomes very small already for $j = 2$ or 3). For clarification, notice that Equations (12) and (14) can be combined such that $n_+ f_j = n_{-j}$. It then follows that Equation (13) is equivalent to a simple charge balance equation, where the equality between $-n_+ + n_{-1} + 2n_{-2} + \ldots$ and $n_i - n_e$ represents overall charge neutrality.

From the formalism of Draine & Sutin (1987), we calculate inverse lifetimes (the "E:s" and "P:s") according to

$$t_x^{-1}(r, \nu, \tau_x) = n_x \sqrt{\frac{8k_B T_x}{\pi m_x}} \pi r^2 J(\nu, \tau_x), \tag{15}$$

where n_x is either n_e or the mass-corrected ion number density θ_C, k_B is Boltzmann's constant, T_x is T_e or the ion temperature, m_x is the electron or proton mass, r is the grain radius, and $J(\nu, \tau_x)$ is a function of ν (the ratio of the charge of the grain and the charge of the attaching species) and τ_x. The latter is a dimensionless parameter referred to as the reduced temperature and given by

$$\tau_x = \frac{4\pi \epsilon_0 k_B r T_x}{q^2}, \tag{16}$$

where ϵ_0 is the permittivity of free space, and q is the elementary charge. The form of J depends on whether the interaction is attractive ($\nu < 0$), neutral ($\nu = 0$), or repulsive ($\nu > 0$):

$$J(\nu, \tau_x) = \begin{cases} (1 - \nu/\tau_x)\left(1 + \sqrt{\frac{2}{\tau_x - 2\nu}}\right) & \nu < 0 \\ 1 + \sqrt{\frac{\pi}{2\tau_x}} & \nu = 0. \\ [1 + (4\tau_x + 3\nu)^{-\frac{1}{2}}]^2 \exp\left(-\frac{\nu}{\tau_x(1 + \nu^{-1/2})}\right) & \nu > 0 \end{cases} \tag{17}$$

For readers who seek to reproduce our results, note, for instance, that calculations with the input $n_e = 5000\,\text{cm}^{-3}$, $T_e = 1500$ K, and $r = 3$ nm give $E_{-2} = t_e^{-1}(\nu = 2) = 8.29 \times 10^{-4}\,\text{s}^{-1}$.
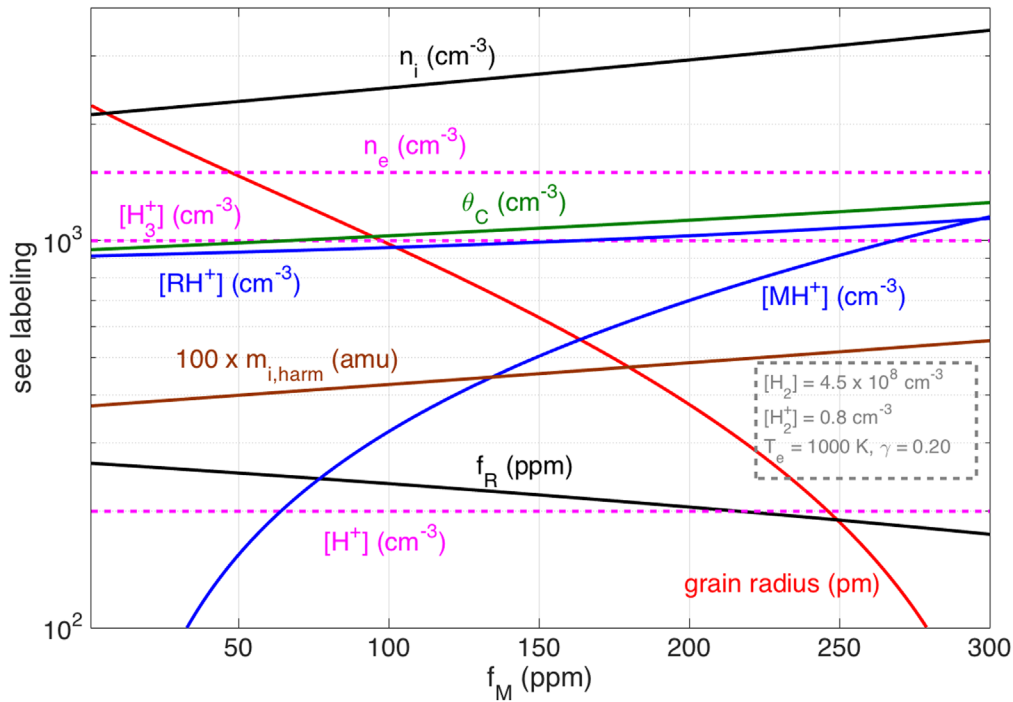
Figure 1. Model results (solid lines) generated by the provided model input (dashed lines and numbers within the text box). In this case, the model has been used for conditions encountered near 2200 km above Saturn's 1 bar level during the inbound part of orbit 292. The [M]/[R] ratio varies over the range 0–~2.

We step the grain size radius by 0.1 Å starting at $r = 1$ Å (which is below the limit where the formalism is applied in Draine & Sutin 1987) until the obtained total electron attachment rate, $R_{e,\text{tot}}$, given by

$$R_{e,\text{tot}} = E_{+}n_{+} + E_{0}n_{0} + E_{-1}n_{-1} + ..., \qquad (18)$$

matches $s_e n_e$, as given by Equation (3). The corresponding grain radius is the one needed for the entire system to be in ionization balance within our theoretical framework (for the results presented in Section 3, we have verified the uniqueness of the solutions).

3. Results and Discussion

The nature of the model output (as can be understood from the figures presented in this work) is such that it is not suitable for being presented in a traditional altitude profile style. We refer readers to Figure (4) in Cravens et al. (2019) for an illustration of how calculated mixing ratios of M- and R-type molecules vary along the trajectory of orbit 288 (as determined empirically without accounting for the possibility of ion and electron attachment to dust particles). Notably, the 288 results from Cravens et al. (2019) display a transition around near-equatorial latitudes (near closest approach), with R-type molecules becoming dominant over M-type molecules. In the following, we apply our model—an extension of the Cravens et al. (2019) model—to two regions probed during the inbound part of Cassini's orbit 292, deliberately targeting locations with significantly different $[\text{H}^+]/[\text{H}_3^+]$ ratios.

### 3.1. Results When Applied to ∼2200 km above the 1 Bar Level during the Inbound Part of Orbit 292

Near ∼2200 km above the 1 bar level (latitude ∼2°–4°N) during the inbound part of Cassini's orbit 292, the following rounded values reasonably match RPWS/LP and INMS

measurements: $n_e = 1.5 \times 10^3 \, \text{cm}^{-3}$, $T_e = 1000$ K, $[\text{H}_2] = 4.5 \times 10^8 \, \text{cm}^{-3}$, $[\text{H}^+] = 200 \, \text{cm}^{-3}$, $[\text{H}_2^+] = 0.8 \, \text{cm}^{-3}$, and $[\text{H}_3^+] = 1000 \, \text{cm}^{-3}$. Insertion into our model renders the output shown in Figure 1.

The mixing ratio of M-type molecules is allowed to be several hundred ppm, and the calculated mixing ratio of R-type molecules also amounts to several hundred ppm. Both of these values are in qualitative agreement with the average mixing ratios reported in Table 2 of Miller et al. (2020), a work discussed further in Section 3.3.1. The total ion number density of ∼3000 cm⁻³ is consistent with RPWS/LP measurements (Morooka et al. 2019), and a dust population with grains of ∼0.5–1 nm radii can explain the electron depletion, at least while the mixing ratio $f_M < 150$ ppm. For $f_M > 200$, the required grain radius quickly drops to values below 3 Å. To this point, it should be noted that Draine & Sutin (1987) applied their grain-charging theory to grains with radii ⩾3 Å. The calculated number density of grains (not shown) remains close to the difference between the calculated ion number density and the electron number density, meaning that the bulk of the grains are singly negatively charged. Another observation to make from Figure 1 is that the calculated $m_{i,\text{harm}}$ is in the range of about 4–5 m_p, which is roughly twice the value inferred from RPWS/LP measurements at the corresponding location (see Figure 2 of Morooka et al. 2019).

3.2. Results When Applied to ∼1700 km above the 1 Bar Level during the Inbound Part of Orbit 292

We have also used the model for conditions encountered near closest approach of the inbound part of Cassini's orbit 292. This corresponds to ∼1700 km above Saturn's 1 bar level and a latitude range of ∼3°–4°S. The following concentrations (rounded values) are utilized and based on previously published data from INMS and RPWS/LP measurements (e.g., Moore et al. 2018; Morooka et al. 2019):
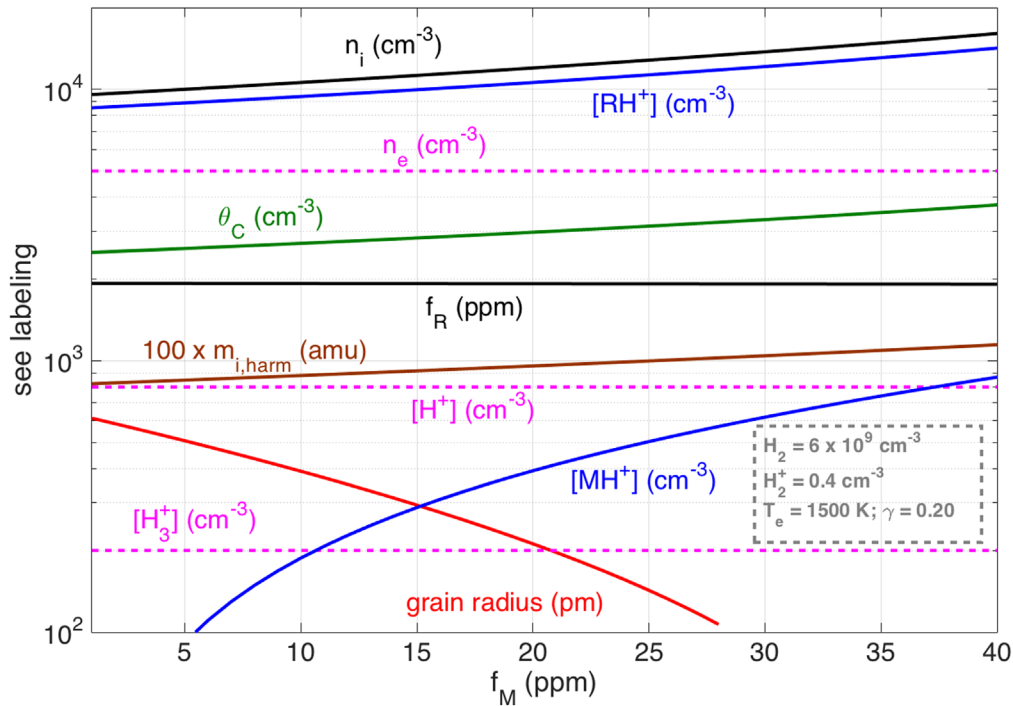
Figure 2. Model results (solid lines) generated by the provided model input (dashed lines and numbers within the text box). In this case, the model has been used for conditions encountered near 1700 km above Saturn's 1 bar level during the inbound part of orbit 292. The [M]/[R] ratio varies over the range 0–∼0.02.

$[H_2] = 6 \times 10^9 \, cm^{-3}$, $n_e = 5 \times 10^3 \, cm^{-3}$, $[H^+] = 800 \, cm^{-3}$, $[H_2^+] = 0.4 \, cm^{-3}$, and $[H_3^+] = 200 \, cm^{-3}$. Moreover, an electron temperature of $T_e = 1500$ K is used based on published RPWS/LP data (Morooka et al. 2019; interestingly, this exceeds the T_e measured near 2200 km). Figure 2 shows how various parameters change with the utilized mixing ratio, f_M, of M-type molecules. The plot extends to the highest value of f_M allowed by our formalism and model input.

Similar to Figure 1, the dashed horizontal lines in Figure 2 represent fixed model input parameters, while the solid lines are model output parameters. The model output suggests a significant level of electron depletion, which is in qualitative agreement with RPWS/LP measurements (Morooka et al. 2019). Again, the dust population is dominated by singly negatively charged particles, and the total dust number density (not shown) is thus close to the difference between the calculated ion number density and the electron number density. The model also predicts the dominance of RH$^+$ ions, which is in line with the work of Dreyer et al. (2021), who proposed that the deep ionosphere is dominated by ion species with comparably low recombination coefficients. However, to this point, it should be noted that the model does not include reactions where MH$^+$ ions are produced at the expense of RH$^+$ ions; see Section 4. The computed $m_{i,harm}$ of ∼10 amu is, again, roughly twice the value of ∼5–6 amu derived from LP sweep analysis in Morooka et al. (2019). At the moment, we refrain from speculating on the cause for the seemingly systematic discrepancy. Instead, we discuss in Section 3.3 two other conundrums: first, in Section 3.3.1, that the mixing ratios of R- and M-type molecules depart significantly from the INMS averages (Miller et al. 2020) and second, in Section 3.3.2, that the grain radius is already forced below 2 Å for M-type mixing ratios exceeding 20 ppm.

3.3. Conundrums Associated with the Results from the Model When Applied to ∼1700 km above the 1 Bar Level during the Inbound Part of Orbit 292

Looking at the variations in T_e and of the input concentrations over a 70 km interval from closest approach, we notice notable departures from the utilized rounded values mainly for [H$^+$] and [H$_3^+$] (see Figure 3 in Moore et al. 2018). We have inspected the model sensitivity to these variations and concluded that the central qualitative conclusions and identified main conundrums persist. However, it should be stressed that we target the inbound of orbit 292 specifically, so the stated input should not be viewed as necessarily typical at near-equatorial latitudes, ∼1700 km above the 1 bar level in Saturn's sunlit atmosphere.

3.3.1. Mixing Ratio Conundrum

We note from Figure 2 that our model suggests an upper limit of the mixing ratio of M-type molecules of ∼40 ppm. The upper limit can be conceived as even lower, since, for $f_M > 28$ ppm, the grain size required to complete the photochemical equilibrium scenario drops below 1 Å. The mixing ratio of R-type molecules is calculated as stable around 2000 ppm. While these mixing ratios seem roughly consistent with the empirical estimates presented for orbit 288 by Cravens et al. (2019; see their Figure 4), they conflict with the average mixing ratio reported from closed-source neutral-mode measurements by the INMS (Perry et al. 2018; Waite et al. 2018; Yelle et al. 2018; Miller et al. 2020). In Table 2 of Miller et al. (2020), H_2O, NH_3, and CH_4 (all M-type molecules) are specified to have average mixing ratios within the range 200–400 ppm, and, specifically for CH_4, a mixing ratio of a few hundred ppm seems to be fairly stable with varying altitude (see Perry et al. 2018; Yelle et al. 2018). For the R-type

molecules, average mixing ratios of $\sim$200 ppm are stated for CO and N_2 in Table 2 of Miller et al. (2020). While it is questionable to compare with average mixing ratios, it seems as if the model generates a mixing ratio of M- and R-type molecules that is roughly an order of magnitude too small and too large, respectively. It can be added that adjusting the assumed mass of MH^+ ions from 19 to 200 amu in the model (connecting back to discussions in Section 2.4) has no notable influence on the model output. Reducing the parameter γ from 0.20 to 0.10 (connecting back to discussions in Section 2.2) mainly has the effect of further reducing the calculated upper limit of M-type molecules down to $\sim$20 ppm.

This mixing ratio conundrum has been highlighted before, although from a slightly different viewpoint. Moore et al. (2018) made use of average mixing ratios of several species (both R- and M-type) as input in their Saturn ionospheric model. The equivalent problem then faced in the output (see their Figure 3) is primarily a poor agreement with observed H^+ and H_3^+ number densities near closest approach; [H^+] is calculated too low and [H_3^+] too high. They stated that some process is required with the propensity of reducing [H_3^+] without reducing [H^+]. We agree on this but with the addition that it would be desirable if the process(es) in question also acted to enhance [H^+].

The collision-induced dissociation (CID) $H_3^+ + H_2 \rightarrow H^+ + 2H_2$ is endoergic by $\sim$4.3 eV and requires significant internal excitation in both reactants to be feasible. We have inspected a simplified chemical scheme, neglecting dust attachment and recombination but adding the CID reaction, and found that an effective rate coefficient of $k_{CID} \sim 3 \times 10^{-12}$ cm^3 s^{-1} yields $f_M \approx f_R \approx 200$ ppm. There are several concerns with such a solution on the mixing ratio conundrum that are so severe that we lean toward ruling out its feasibility. Not only is the required internal excitation indeed substantial, but also, if H_2 is in the fourth vibrational state or higher, it opens up for H^+ loss via $H^+ + H_2(v \geqslant 4) \rightarrow H_2^+ + H$, a process that has historically received a lot of attention in discussions of Saturn's ionization balance (see Moore et al. 2017 and references therein) and that, with reactants in the ground state, is endoergic only by $\sim$1.8 eV.

3.3.2. Grain Size Conundrum

The red solid line in Figure 2 shows the calculated grain size radius that is required to complete a photochemical equilibrium scenario for the ionization balance. Note that the unit is given in pm, and so the resulting radii for $f_M > 20$ ppm remain smaller than 2 Å. Recall that Draine & Sutin (1987) only applied their grain-charging theory to grains with radii $\geqslant$3 Å. We note that a reduction of the ion temperature to values closer to the neutral temperature makes the situation even more problematic. We feel more or less forced to abandon the idea of compact and conducting spherical dust particles acting as the main negative charge carrier in Saturn's deep ionosphere unless drastic flaws prevail in our model input. We intend to study in detail the effect on the model results of introducing size-dependent sticking coefficients for electron- and ion attachment onto grains (at the moment these are set to unity). Another way out may be offered by complex-shaped grains, potentially capable of charging up more negatively than spherical grains of the same size, but we see no simple way of testing this.

The surprisingly rich organic chemistry of Saturn's ionosphere (Perry et al. 2018; Waite et al. 2018) combined with the apparent requirement of "molecular-sized" negative charge carriers motivates us to also explore the option of certain carbon-rich molecules acting as electron attachment sites. The species in question may, for instance, be conceived as a mixture of carbon chains and small polycyclic aromatic hydrocarbons (PAHs), but we are careful not to pinpoint their nature and refer to the hypothesized species collectively as "C-particles." We refer to the number densities of positively charged, neutral, and negatively charged C-particles as n_{C+}, n_C, and n_{C-}, respectively. We set rate constants for various reactions based on a survey of the UMIST database for astrochemistry, inspecting the reactivity of species like C_6H and C_6H_6 and a range of other hydrocarbons. We adapt a rate constant of $k_{ptC} = 2 \times 10^{-9}$ cm^3 s^{-1} for proton transfer from any ion to neutral C-particles, an electron recombination coefficient of $\alpha_{C+} = 5 \times 10^{-7}$ cm^3 s^{-1} for positively charged C-particles, a rate constant of $k_{aC} = 1 \times 10^{-7}$ cm^3 s^{-1} for electron attachment to neutral C-particles, and a rate constant of $k_{MN} = 7 \times 10^{-8}$ cm^3 s^{-1} for the mutual neutralization of negatively charged C-particles with any ion. These (effective) rate constants may very well be off by 50% or even more. We neglect interactions between the C-particles themselves and other processes not mentioned above. Balancing the production and loss rates of positive and negative C-particles and respecting quasi-neutrality renders, respectively,

$$k_{ptC}n_i n_C = \alpha_{C+}n_e n_{C+}, \tag{18a}$$

$$k_{aC}n_e n_C = k_{MN}n_i n_{C-}, \tag{18b}$$

$$n_e + n_{C-} = n_i + n_{C+}. \tag{18c}$$

Approximating $n_i \approx 2n_e = 10{,}000$ cm^{-3} (under the guidance of Figure 2) gives $2k_R n_C = \alpha_C n_{C+}$, $k_d n_C = 2k_{MN}n_{C-}$, $n_{C-} = n_e + n_{C+}$, and, after some algebra, a solution with $n_{C+} = 57$, $n_C = 7080$, and $n_{C-} = 5057$ cm^{-3}. This gives a total concentration of C-particles of $\sim$12,000 cm^{-3}, corresponding to a mixing ratio of 2 ppm. Besides the rather loose notion of C-particles and the uncertainty in effective rate constants, there are several caveats to the crude concentration calculations just made. For instance, the radiative electron attachment to neutral C-particles may possess nonnegligible activation energy barriers, as is suggested to be the case for the electron attachment to C_{60} and possibly also many PAHs (Petrie & Bohme 2000). Also, at least for carbon chain anions, with or without H or N inclusion, a potentially highly competitive loss pathway is through associative electron detachment with atomic hydrogen. Measured rate coefficients for these reactions are on the order of $(5-10) \times 10^{-10}$ cm^3 s^{-1} (Barckholtz et al. 2001; Yang et al. 2010). Considering a mixing ratio of atomic hydrogen possibly as high as $\sim$1% at the pressure level of interest (e.g., Müller-Wodarg et al. 2012; Kim et al. 2014), the loss of negative C-particles through this process may commence up to an $\sim$50 times higher rate than the loss through mutual neutralization, essentially pushing the "required" mixing ratio of the C-particles up to $\sim$100 ppm. On the one hand, such high mixing ratios of organic material are not in conflict with reports from INMS measurements (e.g., Waite et al. 2018; Miller et al. 2020). On the other hand, from a literature/database survey, we have reason to conceive the C-particles as M-type molecules. A mixing ratio of several tens of ppm or more would thus make it even harder to explain the

high H^+ concentration in Saturn's deep ionosphere and further reduce the already "too low" upper limit for the mixing ratios of molecules like H_2O and CH_4. This poses a problem as long as a viable mechanism for enhanced H^+ production (lacking in the model) has not been identified.

Theoretical predictions (Moore et al. 2008; Sakai & Watanabe 2016) suggest that the electron temperature is closer to the neutral temperature at the pressure level of interest. It can be noted that a model run utilizing an electron temperature of $T_e = 370$ K ($\approx$neutral temperature; see, e.g., Yelle et al. 2018) instead of 1500 K causes a reduction in the calculated n_i from >10,000 cm^{-3} to $\sim$6000 cm^{-3}, which is a consequence of the fact that dissociative recombination is more efficient at lower T_e. A reduced level of electron depletion relaxes the requirements on the grain size to complete a self-consistent solution for the ionization balance. However, setting $T_e = 370$ K conflicts with the standard interpretation of the LP sweep characteristics; to this point can be added the fact that the inferred T_e is not particularly sensitive to the fraction of the apparent ion current that is assumed to be caused by impact-induced secondary electron emission.

4. Summary and Concluding Remarks

When applied to conditions encountered near an altitude of $\sim$1700 km above the 1 bar level during the inbound part of orbit 292, our Saturn ionospheric model, which builds on the empirical approach of Cravens et al. (2019), suggests in comparison to INMS measurements (Perry et al. 2018; Waite et al. 2018; Yelle et al. 2018; Miller et al. 2020) too-low mixing ratios of M-type molecules and too-high mixing ratios of R-type molecules. As a reminder, using the terminology of Cravens et al. (2019), M-type molecules (e.g., H_2O, CH_4, and NH_3) are reactive with H^+ and H_3^+, while R-type molecules (CO and N_2) are reactive with H_3^+ but not H^+. Our mixing ratio results are in accord with Cravens et al. (2019), who focused on orbit 288, and the identified conundrum is essentially equivalent to the problem of reproducing the H_3^+ and H^+ number densities in Saturn's deep ionosphere as highlighted in Moore et al. (2018). We considered in Section 3.3.1 the CID of H_3^+, with H_2 as a way of enhancing H^+ production at the expense of H_3^+. An effective rate constant of $k_{CID} \sim 3 \times 10^{-12}$ cm^3 s^{-1} suffices for the calculated mixing ratios of M- and R-type molecules to better match the INMS averages, but we also raised several concerns with this hypothetical solution.

Our model suggests that the total ion number density exceeds the electron number density by a factor of $\sim$2 ($\sim$1700 km above the 1 bar level during the inbound part of orbit 292). This proposes an n_i/n_e ratio of $\sim$50%, which, while low, is higher than the ratio of $\sim$20% reported earlier (see Figure 6 of Morooka et al. 2019). A conundrum arises in that the calculated typical grain radius required for a self-consistent solution becomes smaller than 3 Å, making it difficult to separate them from semicomplex molecules and questionable whether the grain-charging formalism of Draine & Sutin (1987) is even applicable. Ways out of the grain size conundrum were speculated on in Section 3.3.2, but at this stage, we are not in a position to favor any particular explanation.

Drastic modifications made to (artificially) enhance [M] and reduce [R] bring notable changes to the total ion concentration.

This is not surprising, since MH$^+$ ions are characterized by roughly four times higher electron recombination rate constants than RH$^+$ ions. With substantial concentrations of both M- and R-type molecules, the total ion number density is foreseen to be more sensitive to the molecular species that actually dominate the respective population. The maximum total ion number density is realized in a scenario wherein the M-type molecules are heavily dominated by CH_4 and the R-type molecules are dominated by CO. This facilitates effective proton transfer from CH_5^+ to CO and a plasma dominated by HCO$^+$, which has a low recombination constant (bringing this in line with the work of Dreyer et al. 2021). At the other extreme, a high concentration of H_2O and/or NH_3 will render a heavy ion population dominated by H_3O^+ and/or NH_4^+ ions, characterized by markedly higher recombination rate constants than HCO$^+$. Extending the proposed model with a more sophisticated chemical reaction scheme (e.g., Moore et al. 2018) seems a natural way forward.

ORCID iDs

E. Vigren ⓘ https://orcid.org/0000-0003-2647-8259
J. Dreyer ⓘ https://orcid.org/0000-0003-3038-3359
A. I. Eriksson ⓘ https://orcid.org/0000-0003-2926-6761
F. L. Johansson ⓘ https://orcid.org/0000-0002-5386-8255
M. Morooka ⓘ https://orcid.org/0000-0001-9958-0241
J.-E. Wahlund ⓘ https://orcid.org/0000-0002-2107-5859

References

Barckholtz, C., Snow, T. P., & Bierbaum, V. M. 2001, ApJL, 547, L171
Cravens, T. E., Moore, L., Waite, J. H., et al. 2019, GeoRL, 46, 6315
Draine, B. T., & Sutin, B. 1987, ApJ, 320, 803
Dreyer, J., Vigren, E., Morooka, M., et al. 2021, PSJ, 2, 39
Galand, M., Moore, L., Charnay, B., Mueller-Wodarg, I., & Mendillo, M. 2009, JGRA, 114, A06313
Grard, R. J. L., McDonnell, J. A. M., Grün, E., & Gringauz, K. I. 1987, A&A, 187, 785
Hsu, H.-W., Schmidt, J., Kempf, S., et al. 2018, Sci, 362, eaat3185
Huebner, W. F., & Mukherjee, J. 2015, P&SS, 106, 11
Kim, Y. H., Fox, J. L., Black, J. H., & Moses, J. I. 2014, JGRA, 119, 384
Mallik, R. K. 2001, Linear Algebra and its Applications, 325, 109
McElroy, D., Walsh, C., Markwick, A. J., et al. 2013, A&A, 550, A36
Miller, K., Waite, J. H., Perryman, R., et al. 2020, Icar, 339, 113595
Mitchell, D. G., Perry, M. E., Hamilton, D. C., et al. 2018, Sci, 362, eaat2236
Moore, L., Cravens, T. E., Müller-Wodarg, I., et al. 2018, GeoRL, 45, 9398
Moore, L., Galand, M., Kliore, A. J., Nagy, A. F., & O'Donoghue, J. 2017, in Saturn in the 21st Century, ed. K. H. Baines et al. (Cambridge: Cambridge Univ. Press), 196
Moore, L., Galand, M., Mueller-Wodarg, I., Yeller, R., & Mendillo, M. 2008, JGRA, 113, A10306
Morooka, M., Wahlund, J.-E., Hadid, L. Z., et al. 2019, JGRA, 124, 1679
Müller-Wodarg, I. C. F., Moore, L., Galand, M., et al. 2012, Icar, 221, 481
Perry, M. E., Waite, J. H., Jr., Mitchell, D. G., et al. 2018, GeoRL, 45, 10093
Persoon, A. M., Kurth, W. S., Gurnett, D. A., et al. 2019, GeoRL, 46, 3061
Petrie, S., & Bohme, D. K. 2000, ApJ, 540, 869
Sakai, S., & Watanabe, S. 2016, Icar, 274, 261
Wahlund, J.-E., Morooka, M. W., Hadid, L. Z., et al. 2018, Sci, 359, 66
Waite, J. H., Perryman, R. S., Perry, M. E., et al. 2018, Sci, 362, aa2382
Wakelam, V., Loison, J.-C., Herbst, E., et al. 2015, ApJS, 217, 20
Yang, Z., Cole, C. A., Martinez, O., Jr, et al. 2010, ApJ, 739, 19
Yelle, R. V., Serigano, J., Koskinen, T. T., et al. 2018, GeoRL, 45, 10951